TOPOLOGICAL MATTER

Probing topological spin liquids on a programmable quantum simulator

G. Semeghini[1], H. Levine[1], A. Keesling[1,2], S. Ebadi[1], T. T. Wang[1], D. Bluvstein[1], R. Verresen[1], H. Pichler[3,4], M. Kalinowski[1], R. Samajdar[1], A. Omran[1,2], S. Sachdev[1,5], A. Vishwanath[1]*, M. Greiner[1]*, V. Vuletić[6]*, M. D. Lukin[1]*

Quantum spin liquids, exotic phases of matter with topological order, have been a major focus in physics for the past several decades. Such phases feature long-range quantum entanglement that can potentially be exploited to realize robust quantum computation. We used a 219-atom programmable quantum simulator to probe quantum spin liquid states. In our approach, arrays of atoms were placed on the links of a kagome lattice, and evolution under Rydberg blockade created frustrated quantum states with no local order. The onset of a quantum spin liquid phase of the paradigmatic toric code type was detected by using topological string operators that provide direct signatures of topological order and quantum correlations. Our observations enable the controlled experimental exploration of topological matter and protected quantum information processing.

Motivated by theoretical work carried out over the past five decades, a broad search has been underway to identify signatures of quantum spin liquids (QSLs) in correlated materials (1, 2). Moreover, inspired by the intriguing predictions of quantum information theory (3), approaches to engineer such systems for topological protection of quantum information are being actively explored (4). Systems with frustration (5) caused by the lattice geometry or long-range interactions constitute a promising avenue in the search for QSLs. In particular, such systems can be used to implement a class of so-called dimer models (6–10), which are among the most promising candidates to host QSL states. However, realizing and probing such states is challenging because they are often surrounded by other competing phases. Moreover, in contrast to topological systems that involve time-reversal symmetry breaking, such as in the fractional quantum Hall effect (11), these states cannot be easily probed by means of, for example, quantized conductance or edge states. Instead, to diagnose spin liquid phases, it is essential to access nonlocal observables, such as topological string operators (1, 2). Although some indications of QSL phases in correlated materials have been previously reported (12, 13), thus far, these exotic states of matter have evaded direct experimental detection.

Programmable quantum simulators are well suited for the controlled exploration of these strongly correlated quantum phases (14–21). In particular, recent work showed that various phases of quantum dimer models can be efficiently implemented by using Rydberg atom arrays (22) and that a dimer spin liquid state of the toric code type could be potentially created in a specific frustrated lattice (23). Toric code states have been dynamically created in small systems by using quantum circuits (24, 25). However, some of the key properties, such as topological robustness, are challenging to realize in such systems. Spin liquids have also been explored by using quantum annealers, but the lack of coherence in these systems has precluded the observation of quantum features (26).

Dimer models in Rydberg atom arrays

The key idea of our approach is based on a correspondence (23) between Rydberg atoms placed on the links of a kagome lattice (or equivalently, the sites of a ruby lattice) (Fig. 1A) and dimer models on the kagome lattice (8, 10). The Rydberg excitations can be viewed as "dimer bonds" that connect the two adjacent vertices of the lattice (Fig. 1B). Because of the Rydberg blockade (27), strong and properly tuned interactions constrain the density of excitations so that each vertex is touched by a maximum of one dimer. At 1/4 filling, each vertex is touched by exactly one dimer, resulting in a perfect dimer covering of the lattice. Smaller filling fractions result in a finite density of vertices with no proximal dimers, which are referred to as monomers. A QSL can emerge within this dimer-monomer model close to 1/4 filling (23) and can be viewed as a coherent superposition of exponentially many degenerate dimer coverings with a small admixture of monomers (Fig. 1C) (10). This corresponds to the resonating valence bond (RVB)

state (6, 28), which was predicted long ago but is so far still unobserved in any experimental system.

To create and study such states experimentally, we used two-dimensional arrays of 219 ^{87}Rb atoms individually trapped in optical tweezers (29, 30) and positioned on the links of a kagome lattice (Fig. 1A). The atoms were initialized in an electronic ground state $|g\rangle$ and coupled to a Rydberg state $|r\rangle$ by means of a two-photon optical transition with Rabi frequency Ω. The atoms in the Rydberg state $|r\rangle$ interact with one another through a strong van der Waals potential $V = V_0/d^6$, where d is the interatomic distance. This strong interaction prevents the simultaneous excitation of two atoms within a blockade radius $R_b = (V_0/\Omega)^{1/6}$ (27). We adjusted the lattice spacing a and the Rabi frequency Ω so that for each atom in $|r\rangle$, its six nearest neighbors are all within the blockade radius (Fig. 1B), resulting in a maximum filling fraction of 1/4. The resulting dynamics correspond to unitary evolution $U(t)$ governed by the Hamiltonian

$$\frac{H}{\hbar} = \frac{\Omega(t)}{2}\sum_i \sigma_i^x - \Delta(t)\sum_i n_i + \sum_{i<j} V_{ij} n_i n_j \qquad (1)$$

where $\hbar$ is Planck's constant h divided by 2π, $n_i = |r_i\rangle\langle r_i|$ is the Rydberg state occupation at site i, $\sigma_i^x = |g_i\rangle\langle r_i| + |r_i\rangle\langle g_i|$, and $\Delta(t)$ is the time-dependent two-photon detuning. After the evolution, the state was analyzed by means of projective readout of ground-state atoms (Fig. 1A, right) (29).

To explore many-body phases in this system, we used quasi-adiabatic evolution, in which we slowly turned on the Rydberg coupling Ω and subsequently changed the detuning Δ from negative to positive values by using a cubic frequency sweep over ~2 µs (Fig. 1D). We stopped the cubic sweep at different endpoints and first measured the density of Rydberg excitations $\langle n \rangle$. Away from the array boundaries (which result in edge effects permeating just two layers into the bulk), we observed that the average density of Rydberg atoms was uniform across the array (fig. S4) (31). Focusing on the bulk density, we found that for $\Delta/\Omega \gtrsim 3$, the system reaches the desired filling fraction $\langle n \rangle \sim 1/4$ (Fig. 1E, top). The resulting state does not have any obvious spatial order (Fig. 1A) and appears as a different configuration of Rydberg atoms in each experimental repetition (fig. S5) (31). From the single-shot images, we evaluated the probability for each vertex of the kagome lattice to be attached to one dimer (as in a perfect dimer covering), zero dimers (a monomer), or two dimers (representing weak blockade violations). Around $\Delta/\Omega \sim 4$, we observed an approximate plateau at which ~80% of the vertices were connected to a single dimer

(Fig. 1E), indicating an approximate dimer covering.

Measuring topological string operators

A defining property of a phase with topological order is that it cannot be probed locally. Hence, to investigate the possible presence of a QSL state, it is essential to measure nonlocal observables. In the case of dimer models, a particularly convenient set of nonlocal variables is defined in terms of topological string operators, which are analogous to those used in the toric code model (3). For the present model, there are two such string operators, the first of which characterizes the effective dimer description; the second probes quantum coherence between dimer states (23). We first focused on the diagonal operator $Z = \prod_{i \in S} \sigma_i^z$, with $\sigma_i^z = 1 - 2n_i$, which measures the parity of Rydberg atoms along a string S perpendicular to the bonds of the kagome lattice (Fig. 2A). For the smallest closed Z loop, which encloses a single vertex of the kagome lattice, $\langle Z \rangle = -1$ for any perfect dimer covering. Larger loops can be decomposed into a product of small loops around all the enclosed vertices, resulting in
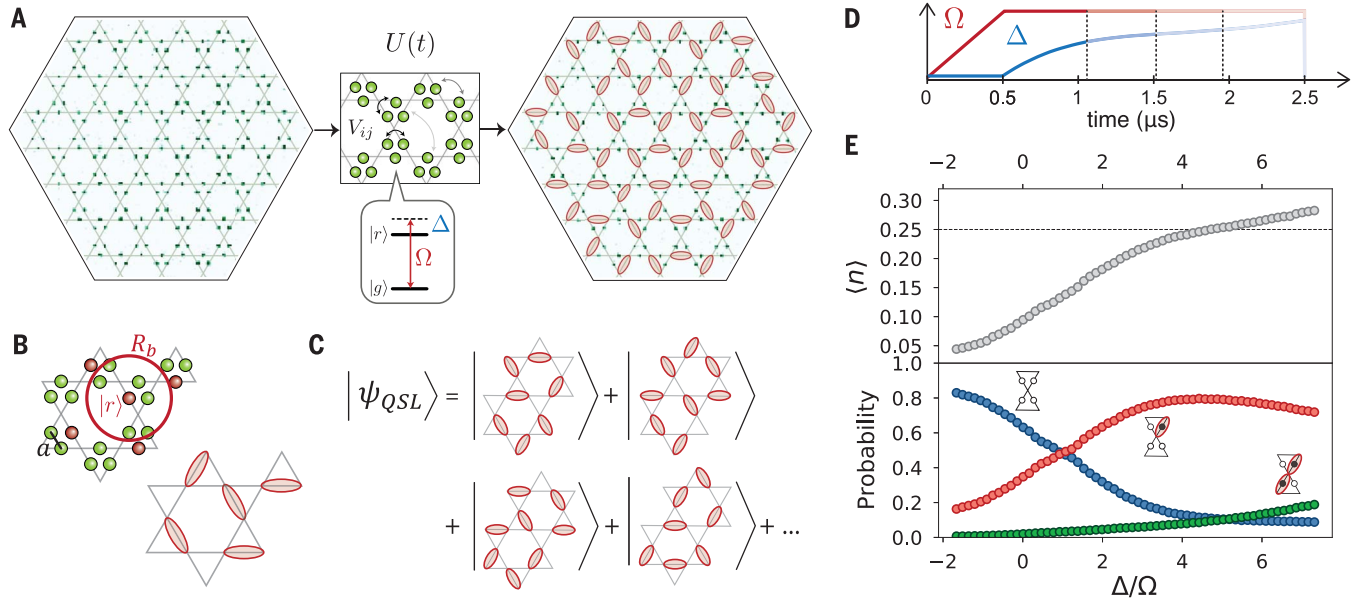

Fig. 1. Dimer model in Rydberg atoms arrays. (**A**) Fluorescence image of 219 atoms arranged on the links of a kagome lattice. The atoms, initially in the ground state $|g\rangle$, evolve according to the many-body dynamics $U(t)$. The final state of the atoms was determined by means of fluorescence imaging of ground-state atoms. Rydberg atoms are indicated with red dimers on the bonds of the kagome lattice. (**B**) We adjusted the blockade radius to $R_b/a = 2.4$ by choosing $\Omega = 2\pi \times 1.4$ MHz and $a = 3.9$ μm, so that all six nearest neighbors of an atom in $|r\rangle$ are within the blockade radius R_b. A state consistent with the Rydberg blockade at maximal filling can then be viewed as a dimer covering of the kagome lattice, where each vertex is touched by exactly one dimer. (**C**) In the idealized limit, the QSL state corresponds to a coherent superposition of exponentially many dimer coverings. (**D**) Detuning $\Delta(t)$ and Rabi frequency $\Omega(t)$ used for quasi-adiabatic state preparation. (**E**) (Top) Average density of Rydberg excitations $\langle n \rangle$ in the bulk of the system, excluding the outer three layers (31). (Bottom) Probabilities of empty vertices in the bulk (monomers; blue symbols), vertices attached to a single dimer (red symbols), or to double dimers (weakly violating blockade; green symbols). After $\Delta/\Omega \sim 3$, the system reaches ~1/4 filling, where most vertices are attached to a single dimer, which is consistent with an approximate dimer phase. The average density of defects per vertex in the approximate dimer phase is ~0.2.
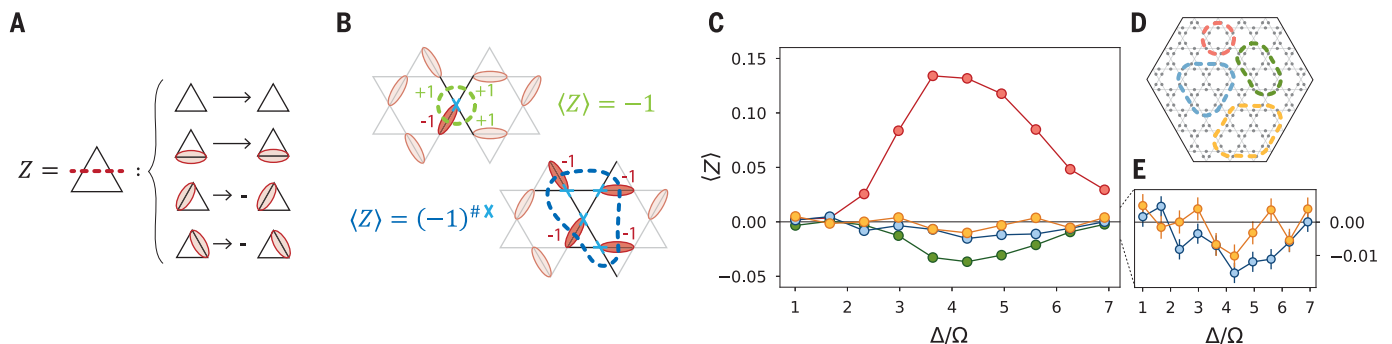
Fig. 2. Detecting a dimer phase by means of diagonal string operator. (**A**) The Z string operator measures the parity of dimers along a string. (**B**) A perfect dimer covering always has exactly one dimer touching each vertex of the array, so that $\langle Z \rangle = (-1)$ around a single vertex and $\langle Z \rangle = (-1)^{\#\text{enclosed vertices}}$ for larger loops. (**C**) Z parity measurements following the quasi-adiabatic sweep of Fig. 1D, with the addition of a 200-ns ramp-down of Ω at the end to optimize preparation. At different endpoints of the sweep and for (**D**) different loop sizes, we measured a finite $\langle Z \rangle$, which is consistent with an approximate dimer phase. The sign of $\langle Z \rangle$ properly matches the parity of the number of enclosed vertices: 6 (red), 11 (green), 15 (blue), and 19 (orange). (**E**) The measured $\langle Z \rangle$ for the two largest loops (fig. S9).
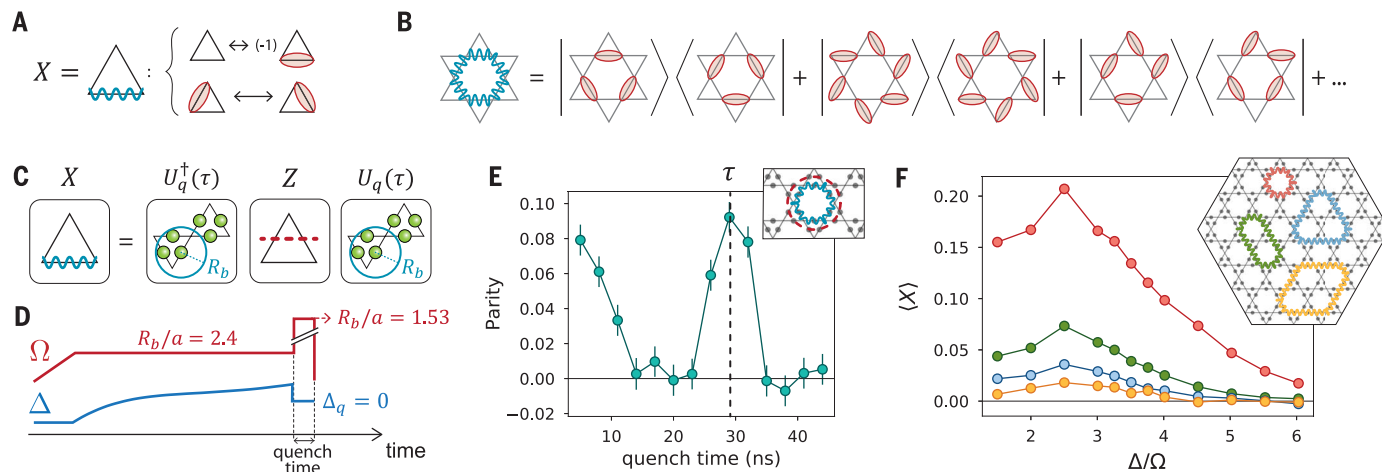
Fig. 3. Probing coherence between dimer states by means of off-diagonal string operator. (**A**) Definition of X string operator on a single triangle of the kagome lattice. (**B**) On any closed loop, the X operator maps any dimer covering into another valid dimer covering, so that $\langle X \rangle$ measures the coherence between pairs of dimer configurations. (**C**) The X operator is measured by evolving the initial state under the Hamiltonian (Eq. 1) with $\Delta = 0$ and reduced blockade radius to encompass only atoms within each individual triangle, implementing a basis rotation that maps X into Z. (**D**) In the experiment, after

the state preparation, we set the laser detuning to $\Delta_q = 0$ and increased Ω to $2\pi \times 20$ MHz to reach $R_b/a = 1.53$. (**E**) By measuring the Z parity on the dual string (red) of a target X loop (blue) after a variable quench time, we identified the time τ for which the mapping in (C) is implemented. (**F**) We measured $\langle X \rangle$ for different final detunings of the cubic sweep and (inset) for different loop sizes and found that the prepared state has long-range coherence that extends over a large fraction of the array (31). The dual Z loops corresponding to the X loops shown in the inset are defined in fig. S3 and (31).

$\langle Z \rangle = (-1)^{\#\text{enclosed vertices}}$ (Fig. 2B). The presence of monomers or double-dimers reduces the effective contribution of each vertex, resulting in a reduced $\langle Z \rangle$.

To measure $\langle Z \rangle$ for different loop shapes (Figs. 2, C and D), we evaluated the string observables directly from single-shot images, averaging over many experimental repetitions and over all loops of the same shape in the bulk of the lattice (31). In the range of detunings where $\langle n \rangle \sim 1/4$, we clearly observed the emergence of a finite $\langle Z \rangle$ for all loop shapes, with the sign matching the parity of enclosed vertices, as expected for dimer states (Fig. 2B). The measured values were generally $|\langle Z \rangle| < 1$ and decreased with increasing loop size, suggesting the presence of a finite density of defects. Nevertheless, these observations indicate that the state we prepared was consistent with an approximate dimer phase.

We next explored quantum coherence properties of the prepared state. To this end, we considered the off-diagonal X operator, which acts on strings along the bonds of the kagome lattice. It is defined in Fig. 3A by its action on a single triangle (23). Applying X on any closed string maps a dimer covering to another valid dimer covering (for example, a loop around a single hexagon in Fig. 3B). A finite expectation value for X therefore implies that the state contains a coherent superposition of one or more pairs of dimer states coupled by that specific loop, which is a prerequisite for a QSL. The measurement of X can be implemented by performing a collective basis rotation, illustrated in Fig. 3C (23). This rotation was implemented

through time evolution under the Rydberg Hamiltonian (Eq. 1) with $\Delta = 0$ and reduced blockade radius $R_b/a = 1.53$, so that only the atoms within the same triangle were subject to the Rydberg blockade constraint. Under these conditions, it was sufficient to consider the evolution of individual triangles separately, where each triangle can be described as a four-level system ($\triangle, \triangle, \triangle, \triangle$). Within this subspace, after a time $\tau = 4\pi/(3\Omega\sqrt{3})$, the collective three-atom dynamics realizes a unitary U_q that implements the basis rotation that transforms an X string into a dual Z string (31).

Experimentally, the basis rotation was implemented after the state preparation by quenching the laser detuning to $\Delta_q = 0$ and increasing the laser intensity by a factor of $\sim$200 to reduce the blockade radius to $R_b/a = 1.53$ (Fig. 3D) (31). We calibrated τ by preparing the state at $\Delta/\Omega = 4$ and evolving under the quench Hamiltonian for a variable time. We measured the parity of a Z string that was dual to a target X loop and observed a sharp revival of the parity signal at $\tau \sim 30$ ns (Fig. 3E) (23). Fixing the quench time τ, we measured $\langle X \rangle$ for different values of the detuning Δ at the end of the cubic sweep (Fig. 3F) and observed a finite X parity signal for loops that extend over a large fraction of the array. These observations clearly indicate the presence of long-range coherence in the prepared state.

Probing spin liquid properties

The study of closed string operators showed that we prepared an approximate dimer phase

with quantum coherence between dimer coverings. Although these closed loops are indicative of topological order, we needed to compare their properties with those of open strings to distinguish topological effects from trivial ordering—the former being sensitive to the topology of the loop (32–34). This comparison is shown in Fig. 4, D and E, and indicates several distinct regimes. For small Δ, we found that both Z and X loop parities factorize into the product of the parities on the half-loop open strings; in particular, the finite $\langle Z \rangle$ is a trivial result of the low density of Rydberg excitations. By contrast, loop parities no longer factorize in the dimer phase ($3 \lesssim \Delta/\Omega \lesssim 5$). Instead, the expectation values for both open string operators vanish in the dimer phase, indicating the nontrivial nature of the correlations measured with the closed loops (31). More specifically, topological ordering in the dimer-monomer model can break down either because of a high density of monomers, corresponding to the trivial disordered phase at small Δ/Ω, or owing to the lack of long-range resonances, corresponding to a valence bond solid (VBS) (23). Open Z and X strings distinguish the target QSL phase from these proximal phases: When normalized according to the definition from Fredenhagen and Marcu (FM) (Fig. 4, B and C) (32, 33), vanishing expectation values for these open strings can be considered to be key signatures for the QSL. In particular, open Z strings have a finite expectation value when the dimers form an ordered spatial arrangement, as in the VBS phase. At the same time, open X strings create pairs

of monomers at their endpoints (Fig. 4A), so a finite $\langle X \rangle$ can be achieved in the trivial phase, where there is a high density of monomers. Therefore, the QSL can be identified as the only phase where both FM string order parameters vanish for long strings (23).

The measured values of the FM order parameters are shown in Fig. 4, F and G. We found that $\langle Z \rangle_{FM}$ is compatible with zero over the entire range of Δ/Ω, where we observed a finite Z parity on closed loops, indicating the absence of a VBS phase (Fig. 4F), which is consistent with our analysis of density-density correlations (fig. S6) (31). At the same time, $\langle X \rangle_{FM}$ converges toward zero on the longest strings for $\Delta/\Omega \gtrsim 3.3$ (Fig. 4G), indicating a transition out of the disordered phase. By combining these two measurements with the regions of nonvanishing parity for the closed Z and X loops (Figs. 2 and 3), we conclude that for $3.3 \lesssim \Delta/\Omega \lesssim 4.5$, our results constitute a direct detection of the onset of a QSL phase (Fig. 4, F and G, shaded area).

The measurements of the closed-loop operators in Figs. 2 and 3 show that $|\langle Z \rangle|, |\langle X \rangle| < 1$ and that the amplitude of the signal decreases with increasing loop size, which results from a finite density of quasiparticle excitations. Specifically, defects in the dimer covering such as monomers and double-dimers can be interpreted as electric (e) anyons in the language of lattice gauge theory (23). Because the presence of a defect inside a closed loop changes the sign of Z, the parity on the loop is reduced according to the number of enclosed e-anyons as $|\langle Z \rangle| = \left| \left\langle (-1)^{\#\text{enclosed } e\text{–anyons}} \right\rangle \right|$. The average number of defects inside a loop is expected to scale with the number of enclosed vertices—with the area of the loop—and we observed an approximate area-law scaling of $|\langle Z \rangle|$ for small loop sizes (Fig. 4H). However, for larger loops we observed a deviation from area-law scaling, closer to a perimeter law. This can emerge if pairs of anyons are correlated over a characteristic length scale smaller than the loop size [a discussion of the expected scaling is provided in (31)]. Pairs of correlated anyons that are both inside the loop do not change its parity because their contributions cancel out; they only affect $\langle Z \rangle$ when they sit across the loop, leading to a scaling with the length of the perimeter. These pairs can be viewed as resulting from the application of X string operators to a dimer covering (Fig. 4A), originating, for example, from virtual excitations in the dimer-monomer model (31) or from errors caused by state preparation and detection. State preparation with larger Rabi frequency (improved adiabaticity) results in larger Z parity signals and reduced e-anyon density (fig. S9).

A second type of quasiparticle excitation that could arise in this model is the so-called

magnetic (m) anyon. Analogous to e-anyons, which live at the endpoints of open X strings (Fig. 4A), m-anyons are created by open Z strings and correspond to phase errors between dimer coverings (fig. S11) (31). These excitations cannot be directly identified from individual snapshots but are detected with the measurement of closed X loop operators. The perimeter law scaling observed in Fig. 4I indicates that m-anyons only appear in pairs

with short correlation lengths (31). These observations highlight the prospects for using topological string operators to detect and probe quasiparticle excitations in the system.

Toward a topological qubit

To further explore the topological properties of the spin liquid state, we created an atom array with a small hole by removing three atoms on a central triangle (Fig. 5), which creates
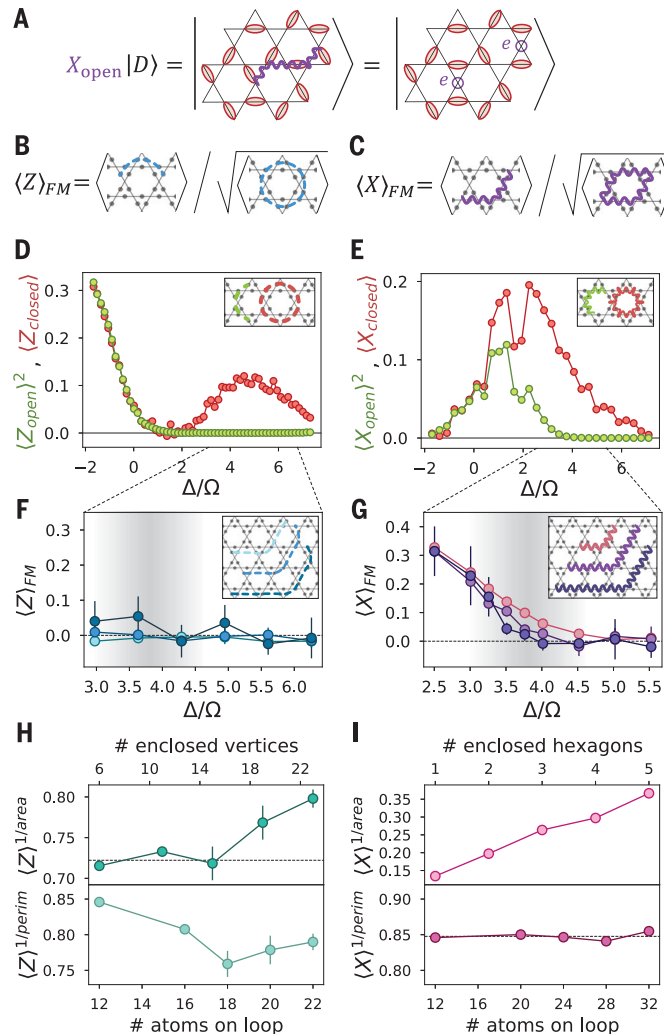
Fig. 4. String order parameters and quasi-particle excitations. (**A**) An open string operator X_{open} acting on a dimer state $|D\rangle$ creates two monomers (e-anyons) at its endpoints (m-anyons are shown in fig. S11). (**B** and **C**) Definition of the string order parameters $\langle Z \rangle_{FM}$ and $\langle X \rangle_{FM}$. (**D**) Comparison between $\langle Z_{\text{closed}} \rangle$ and $\langle Z_{\text{open}} \rangle^2$ measured on the strings shown in the inset. The expectation value shown for the open string is squared to account for a factor of two in the string lengths. (**E**) Analogous comparison for X. (**F** and **G**) Zooming in on the range with finite closed loop parities, we measured the FM order parameters for different open strings (insets). We found that $\langle Z \rangle_{FM}$ is consistent with zero over the entire range of Δ, whereas $\langle X \rangle_{FM}$ vanishes for $\Delta/\Omega \gtrsim 3.3$, which allowed us to identify a range of detunings consistent with the onset of a QSL phase (shaded area). (**H**) Rescaled parities $\langle Z \rangle^{1/\text{area}}$ and $\langle Z \rangle^{1/\text{perim}}$ evaluated for $\Delta/\Omega = 3.6$, where area and perimeter are defined as the number of vertices enclosed by the loop and the number of atoms on the loop, respectively. For small loops, Z scales with an area law but deviates from this behavior for larger loops, converging toward a perimeter law. (**I**) $\langle X \rangle^{1/\text{area}}$ (the area, in this case, is the number of enclosed hexagons) and $\langle X \rangle^{1/\text{perim}}$ evaluated for $\Delta/\Omega = 3.5$, indicating an excellent agreement with a perimeter-law scaling.
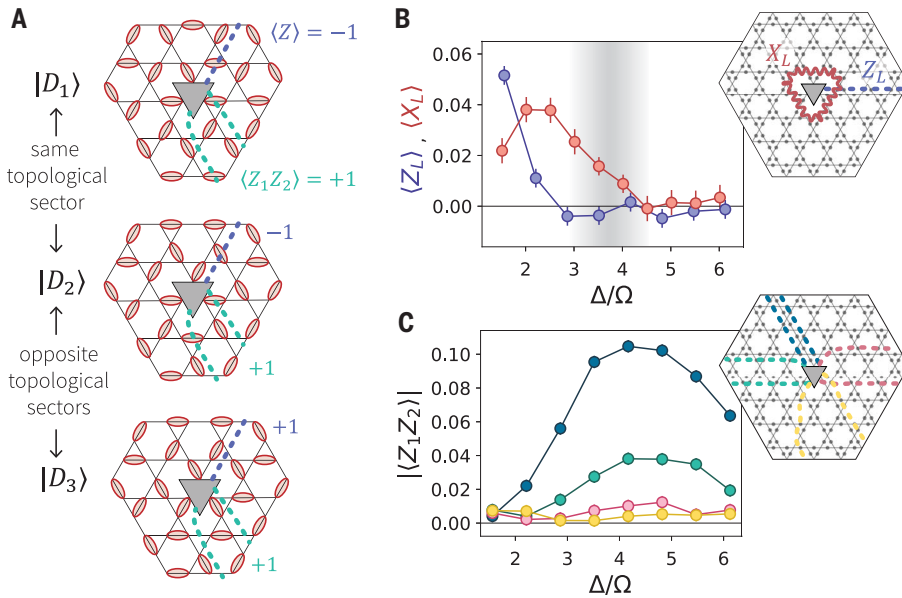
Fig. 5. Topological properties in array with a hole. (A) A lattice with nontrivial topology is obtained by removing three atoms at the center to create a small hole. The dimer states can be divided into two distinct topological sectors 0 and 1. Z strings connecting the hole to the boundary always have a well-defined expectation value within each sector and opposite sign between the two sectors; the correlations between two such strings $Z_1 Z_2$ are identical for both sectors. **(B)** Measured expectation values for the operators Z_L and X_L, defined in the inset, indicate that in the QSL region (shaded area), we prepared a superposition state of the two topological sectors ($\langle Z_L \rangle = 0$) with a finite overlap with the $|+\rangle$ state ($\langle X_L \rangle > 0$). **(C)** Finite expectation values for the correlations between pairs of hole-to-boundary Z strings (inset), which is consistent with (A).

an effective inner boundary [both inner and outer boundaries here correspond to the so-called m-type boundaries (*31*)]. This resulted in two distinct topological sectors for the dimer coverings, where states belonging to different sectors can be transformed into each other only through large X loops that enclose the hole, constituting a highly nonlocal process (involving at least a 16-atom resonance) (fig. S13). We define the logical states $|0_L\rangle$ and $|1_L\rangle$ as the superpositions of all dimer coverings from the topological sectors 0 and 1, respectively. One can define (*23*) the logical operator σ_L^z as being proportional to any Z_L string operator that connects the hole with the outer boundary, given that these have a well-defined eigenvalue ±1 for all dimer states in the same sector but opposite for the two sectors. The logical σ_L^x is instead proportional to X_L, which is any X loop around the hole. This operator anticommutes with Z_L and has eigenstates $|+\rangle \sim (|0_L\rangle + |1_L\rangle)/\sqrt{2}$ and $|-\rangle \sim (|0_L\rangle - |1_L\rangle)/\sqrt{2}$.

We measured Z_L and X_L on the strings defined in Fig. 5B, inset, following the same quasi-adiabatic preparation as in Fig. 1D. We found that in the range of Δ/Ω associated with the onset of a QSL phase, $\langle Z_L \rangle = 0$, and $\langle X_L \rangle > 0$, indicating that the system is in a superposition of the two topological sectors, with a finite overlap with the $|+\rangle$ state (Fig. 5B), which is consistent with the symmetric

initial state and the quasi-adiabatic preparation procedure (*31*). To further support this conclusion, we evaluated correlations $\langle Z_1 Z_2 \rangle$ between hole-to-boundary strings, which are expected to have the same expectation values for both topological sectors (Fig. 5A). In agreement with this prediction, we found that the correlations between different pairs of strings have finite expectation values, with amplitudes decreasing with the distance between the strings (Fig. 5C) owing to imperfect state preparation. These measurements represent the first steps toward initialization and measurement of a topological qubit in our system.

Discussion and outlook

It is not possible to classically simulate quantum dynamics for the full experimental system, so we compare our results with several theoretical approaches. First, our observations qualitatively disagree with the ground-state phase diagram obtained from density-matrix-renormalization-group (DMRG) (*35*, *36*) simulations on infinitely long cylinders. For the largest accessible system sizes, including van der Waals interactions only up to intermediate distances (~$4a$), we found a $\mathbb{Z}_2$ spin liquid in the ground state (fig. S15). However, unlike in deformed lattices (*23*), longer-range couplings destabilize the spin liquid in the ground state

of the Hamiltonian (Eq. 1) on the specific ruby lattice used in the experiment, leading to a direct first-order transition from the disordered phase to the VBS phase (figs. S15 and S16). By contrast, we experimentally observed the onset of the QSL phase in a relatively large parameter range, and no signatures of a VBS phase were detected.

To develop additional insight, we performed time-dependent DMRG calculations (*35–37*) that simulated the same state preparation protocol as in the experiment on an infinitely long cylinder with a seven-atom-long circumference (*31*). The results of these simulations are in good qualitative agreement with our experimental observations (fig. S19). Specifically, similar to the results in Fig. 4, in the region $\frac{\Delta}{\Omega} \sim 3.5$ to 4.5 we found nonzero signals for closed Z and X loops, which cannot be factorized into open strings (fig. S19). Consistent with experimental observations, these indicate the onset of spin liquid correlations. In addition, exact diagonalization studies of a simplified blockade model reveal how the dynamical state preparation creates an approximate equal-weight and equal-phase superposition of many dimer states, instead of the VBS ground state (*31*). We conclude that quasi-adiabatic state preparation occurring over a few microseconds is insensitive to longer-range couplings and generates states that retain the QSL character (*31*). Although this phenomenon deserves further theoretical studies, these considerations indicate the creation of a metastable state with key characteristic properties of a QSL.

Our experiments offer detailed insights into elusive topological quantum matter. These studies can be extended along a number of directions, including improvement of the robustness of the QSL by using modified lattice geometries and boundaries (*22*, *23*) as well as optimization of the state preparation to minimize quasiparticle excitations; understanding and mitigation of environmental effects associated, for example, with dephasing and spontaneous emission (*31*); and optimization of string operator measurements by using quasi-local transformations (*38*), potentially with the help of quantum algorithms (*39*). At the same time, hardware-efficient techniques for robust manipulation and braiding of topological qubits can be explored. Furthermore, methods for anyon trapping and annealing can be investigated, with eventual applications toward fault-tolerant quantum information processing (*40*). With improved programmability and control, a broader class of topological quantum matter and lattice gauge theories can be efficiently implemented (*41*, *42*), opening the door to their detailed exploration under controlled experimental conditions and providing a route for the design of quantum materials that can supplement exactly

solvable models (*3, 43*) and classical numerical methods (*35, 36*).

Note added in proof: During the completion of this manuscript, we became aware of related work demonstrating the preparation of toric code states by using quantum circuits on a superconducting processor (*44*).

REFERENCES AND NOTES

1. X.-G. Wen, *Rev. Mod. Phys.* **89**, 041004 (2017).
2. S. Sachdev, *Rep. Prog. Phys.* **82**, 014001 (2019).
3. A. Kitaev, *Ann. Phys.* **303**, 2–30 (2003).
4. C. Nayak, S. H. Simon, A. Stern, M. Freedman, S. Das Sarma, *Rev. Mod. Phys.* **80**, 1083–1159 (2008).
5. L. Savary, L. Balents, *Rep. Prog. Phys.* **80**, 016502 (2017).
6. D. S. Rokhsar, S. A. Kivelson, *Phys. Rev. Lett.* **61**, 2376–2379 (1988).
7. N. Read, S. Sachdev, *Phys. Rev. Lett.* **66**, 1773–1776 (1991).
8. S. Sachdev, *Phys. Rev. B Condens. Matter* **45**, 12377–12396 (1992).
9. R. Moessner, S. L. Sondhi, *Phys. Rev. Lett.* **86**, 1881–1884 (2001).
10. G. Misguich, D. Serban, V. Pasquier, *Phys. Rev. Lett.* **89**, 137202 (2002).
11. B. I. Halperin, J. K. Jain, *Fractional Quantum Hall Effects* (World Scientific, 2020).
12. T.-H. Han *et al.*, *Nature* **492**, 406–410 (2012).
13. M. Fu, T. Imai, T.-H. Han, Y. S. Lee, *Science* **350**, 655–658 (2015).
14. C. Gross, I. Bloch, *Science* **357**, 995–1001 (2017).
15. H. Weimer, M. Müller, I. Lesanovsky, P. Zoller, H. P. Büchler, *Nat. Phys.* **6**, 382–388 (2010).
16. M. Hermele, V. Gurarie, A. M. Rey, *Phys. Rev. Lett.* **103**, 135301 (2009).
17. N. Y. Yao *et al.*, *Phys. Rev. Lett.* **110**, 185302 (2013).
18. A. W. Glaetzle *et al.*, *Phys. Rev. X* **4**, 041037 (2014).
19. A. Celi *et al.*, *Phys. Rev. X* **10**, 021057 (2020).
20. S. de Léséleuc *et al.*, *Science* **365**, 775–780 (2019).
21. T. Ozawa *et al.*, *Rev. Mod. Phys.* **91**, 015006 (2019).
22. R. Samajdar, W. W. Ho, H. Pichler, M. D. Lukin, S. Sachdev, *Proc. Natl. Acad. Sci. U.S.A.* **118**, e2015785118 (2021).
23. R. Verresen, M. D. Lukin, A. Vishwanath, *Phys. Rev. X* **11**, 031005 (2021).
24. C. Song *et al.*, *Phys. Rev. Lett.* **121**, 030502 (2018).
25. C. K. Andersen *et al.*, *Nat. Phys.* **16**, 875–880 (2020).
26. S. Zhou, D. Green, E. D. Dahl, C. Chamon, *Phys. Rev. B* **104**, L081107 (2021).
27. M. Saffman, T. G. Walker, K. Mølmer, *Rev. Mod. Phys.* **82**, 2313–2363 (2010).
28. P. Anderson, *Mater. Res. Bull.* **8**, 153–160 (1973).
29. S. Ebadi *et al.*, *Nature* **595**, 227–232 (2021).
30. P. Scholl *et al.*, *Nature* **595**, 233–238 (2021).
31. Materials and methods are available as supplementary materials.
32. K. Fredenhagen, M. Marcu, *Commun. Math. Phys.* **92**, 81–119 (1983).
33. J. Bricmont, J. Frölich, *Phys. Lett. B* **122**, 73–77 (1983).
34. K. Gregor, D. A. Huse, R. Moessner, S. L. Sondhi, *New J. Phys.* **13**, 025009 (2011).
35. S. R. White, *Phys. Rev. Lett.* **69**, 2863–2866 (1992).
36. J. Hauschild, F. Pollmann, *SciPost Phys. Lect. Notes* p. 5 (2018).
37. M. P. Zaletel, R. S. K. Mong, C. Karrasch, J. E. Moore, F. Pollmann, *Phys. Rev. B Condens. Matter Mater. Phys.* **91**, 165112 (2015).
38. M. B. Hastings, X.-G. Wen, *Phys. Rev. B Condens. Matter Mater. Phys.* **72**, 045141 (2005).
39. I. Cong, S. Choi, M. D. Lukin, *Nat. Phys.* **15**, 1273–1278 (2019).
40. E. Dennis, A. Kitaev, A. Landahl, J. Preskill, *J. Math. Phys.* **43**, 4452–4505 (2002).
41. M. C. Bañuls *et al.*, *Eur. Phys. J. D* **74**, 165 (2020).
42. L. Tagliacozzo, A. Celi, A. Zamora, M. Lewenstein, *Ann. Phys.* **330**, 160–191 (2013).
43. A. Kitaev, *Ann. Phys.* **321**, 2–111 (2006).
44. K. J. Satzinger *et al.*, *Science* **374**, 1237–1241 (2021).
45. G. Semeghini *et al.*, Probing topological spin liquids on a programmable quantum simulator. *Harvard Dataverse* (2021); doi:10.7910/DVN/BDCTRX.
46. R. Verresen, rubenverr/DMRG-QSL-Rydberg-experiment. Zenodo (2021); doi:10.5281/zenodo.5553679.

Science

Probing topological spin liquids on a programmable quantum simulator

G. SemeghiniH. LevineA. KeeslingS. EbadiT. T. WangD. BluvsteinR. VerresenH. PichlerM. KalinowskiR. SamajdarA. OmranS. SachdevA. VishwanathM. GreinerV. Vuleti#M. D. Lukin

Synthesizing topological order

Topologically ordered matter exhibits long-range quantum entanglement. However, measuring this entanglement in real materials is extremely tricky. Now, two groups take a different approach and turn to synthetic systems to engineer the topological order of the so-called toric code type (see the Perspective by Bartlett). Satzinger *et al.* used a quantum processor to study the ground state and excitations of the toric code. Semeghini *et al.* detected signatures of a toric code–type quantum spin liquid in a two-dimensional array of Rydberg atoms held in optical tweezers. —JS

View the article online
https://www.science.org/doi/10.1126/science.abi8794
Permissions
https://www.science.org/help/reprints-and-permissions

Use of this article is subject to the Terms of service